Research Article

Entropy regulation in LaNbO$_4$-based fergusonite to implement high-temperature phase transition and promising dielectric properties

Deqin Chen[a], Na Yan[a], Xuefeng Cao[a], Fengrong Li[a], Laijun Liu[a],
Qinghua Shen[b], Huanfu Zhou[a], Chunchun Li[a,b,*]

[a]*Guangxi University Key Laboratory of Non-ferrous Metal Oxide Electronic Functional Materials and Devices, College of Material Science and Engineering, Guilin University of Technology, Guilin 541004, China*
[b]*Guangxi Key Laboratory of Embedded Technology and Intelligent System, Guilin University of Technology, Guilin 541004, China*

Abstract: High-entropy effect is a novel design strategy to optimize properties and explore novel materials. In this work, (La$_{1/5}$Nd$_{1/5}$Sm$_{1/5}$Ho$_{1/5}$Y$_{1/5}$)NbO$_4$ (5RNO) high-entropy microwave dielectric ceramics were successfully prepared in the sintering temperature (S.T.) range of 1210–1290 ℃ via a solid-phase reaction route, and medium-entropy (La$_{1/3}$Nd$_{1/3}$Sm$_{1/3}$)NbO$_4$ and (La$_{1/4}$Nd$_{1/4}$Sm$_{1/4}$Ho$_{1/4}$)NbO$_4$ (3RNO and 4RNO) ceramics were compared. The effects of the entropy (*S*) on crystal structure, phase transition, and dielectric performance were evaluated. The entropy increase yields a significant increase in a phase transition temperature (from monoclinic fergusonite to tetragonal scheelite structure). Optimal microwave dielectric properties were achieved in the high-entropy ceramics (5RNO) at the sintering temperature of 1270 ℃ for 4 h with a relative density of 98.2% and microwave dielectric properties of dielectric permittirity (ε_r) = 19.48, quality factor ($Q \times f$) = 47,770 GHz, and resonant frequency temperature coefficient (τ_f) = –13.50 ppm/℃. This work opens an avenue for the exploration of novel microwave dielectric material and property optimization via entropy engineering.

Keywords: high-entropy ceramics; microwave dielectric property; ion disorder; far-infrared

1 Introduction

Microwave dielectric ceramics are indispensable materials in the field of communication, which are widely used in mobile communication, radar, satellite positioning, and navigation systems [1,2]. With the advent of the fifth-generation (5G)/sixth-generation (6G) communication era, higher requirements are put forward for microwave dielectric materials. There are three main parameters used to measure the properties of the microwave dielectric ceramics, i.e., dielectric permittirity (ε_r, mainly contributed by ion displacement polarization and electron displacement polarization), quality factor ($Q \times f$, used to measure energy loss of

* Corresponding author.
E-mail: lichunchun2003@126.com

ceramics in polarization states ($Q = 1/\tan\delta$), where $\tan\delta$ is the dielectric loss), and resonant frequency temperature coefficient (τ_f, resonance frequency shift in different temperatures (T) of ceramics). Electronic equipment with microwave resonators requires high $Q\times f$ ($\geqslant 10{,}000$ GHz) and near-zero $|\tau_f|$ ($\leqslant 10$ ppm/℃) [3,4]. High ε_r (> 50) are conducive to the miniaturization of microwave components, while low ε_r ($\leqslant 20$) enable fast signal propagation [5]. However, because of the trade-off among three parameters, the exploration of materials with excellent microwave dielectric properties is still in progress.

"High entropy" refers to the solution of five or more atoms at one Wyckoff site [6]. The configuration entropy (S_c) of the system can be calculated by Eq. (1) [7]:

$$S_c = -R\sum_{i=1}^{n} x_i \ln x_i \qquad (1)$$

where x_i is the concentration of the ith component, and R is the gas constant in the ideal state. According to the magnitude of the S_c value, the system is generally divided into low entropy ($S_c \leqslant 1.0R$), medium entropy ($1.0R < S_c \leqslant 1.5R$), and high entropy ($S_c > 1.5R$) [8,9]. Gibbs free energy ($\Delta G = \Delta H - T\Delta S$, where H is the enthalpy, and S is the entropy) of the system decreases with the increase in the entropy, which improves structural stability. In addition, H is conducive to an orderly arrangement of ions, and the entropy promotes the disorder of the ions. In 2015, inspired by high-entropy alloys, Rost *et al.* [10] first proposed the concept of high-entropy oxides and successfully prepared (Mg,Co,Ni,Cu,Zn)O with a rock salt structure. Subsequently, the high-entropy ceramics have been extended to carbides, borides, and silicates, and are still being enriched [11–13]. The outstanding performance of high-entropy compounds in thermodynamic and electrical properties is ascribed to the high-entropy effect [14].

At present, the high-entropy effect has been introduced into the dielectric materials to adjust the properties. For example, good stability in ε_r was reported in high-entropy perovskite Ba(Zr$_{0.2}$Ti$_{0.2}$Sn$_{0.2}$Hf$_{0.2}$Me$_{0.2}$)O$_3$ (Me = Nb^{5+}, Ta^{5+}) ceramics over a wide temperature range (30–200 ℃) along with low $\tan\delta$ [15]. Xie *et al.* [16] reported a giant ε_r (~320,000 at 642 ℃ and 100 Hz) in (La$_{0.2}$Pr$_{0.2}$Nd$_{0.2}$Sm$_{0.2}$Eu$_{0.2}$)$_2$Ce$_2$O$_7$ high-entropy ceramics with a defect fluorite structure. Xiang *et al.* [17] prepared Li(Gd$_{0.2}$Ho$_{0.2}$Er$_{0.2}$Yb$_{0.2}$Lu$_{0.2}$)GeO$_4$ microwave dielectric ceramics via high-entropy solid solubility

and optimized the microwave dielectric properties ($\varepsilon_r = 7.6$, $Q\times f = 11{,}700$ GHz, and $\tau_f = -7.4$ ppm/℃). Liu *et al.* [18] prepared olivine structured (Mg$_{0.2}$Ni$_{0.2}$Zn$_{0.2}$Co$_{0.2}$Mn$_{0.2}$)$_2$SiO$_4$ high-entropy ceramics with the optimal microwave dielectric properties ($\varepsilon_r = 8.02$, $\tan\delta = 5.1\times10^{-4}$ at 14.5 GHz, and $\tau_f = -38.2$ ppm/℃). Recently, Ding *et al.* [19] successfully prepared (Hf$_{0.25}$Zr$_{0.25}$Sn$_{0.25}$Ti$_{0.25}$)O$_2$ high-entropy ceramics (with the microwave dielectric properties of $\varepsilon_r = 25.6$, $Q\times f = 74{,}600$ GHz, and $\tau_f = -47$ ppm/℃). They believe that the (Hf$_{0.25}$Zr$_{0.25}$Sn$_{0.25}$Ti$_{0.25}$)O$_2$ ceramics are like (Zr,Sn)TiO$_4$ ceramics [20,21], and $Q\times f$ increases with ion disorder. It is improved compared with that of Hf$_{0.5}$Ti$_{0.5}$O$_2$ (~53,600 GHz) [22].

Rare-earth niobates, with a general formula of RENbO$_4$, have been intensely studied because of their unique tetrahedral coordination with oxygen for Nb^{5+} and the reversible ferroelastic phase transitions from low-temperature fergusonite (monoclinic, $C2/c$) to high-temperature scheelite structure (tetragonal, $I4_1/a$) [23,24]. RENbO$_4$ has been explored to promote their prospects in microwave or millimeter wave communications owing to their qualifying microwave dielectric properties. For example, Kim *et al.* [25] reported the microwave dielectric properties of RENbO$_4$ (RE = La, Nd, Sm, Dy, Er, and Lu) with low ε_r (= 16.6–19.6) and high $Q\times f$ (= 33,000–56,600 GHz). Of particular interest is the jumping in the τ_f values from positive (~9 ppm/℃ in LaNbO$_4$) to largely negative (~−64 ppm/℃ for LuNbO$_4$) with the decreasing ionic radius in rare-earth elements, which was explained by the lattice distortion caused by phase transformation. Because of their high $Q\times f$, they have stable frequency selection characteristics in microwave. Therefore, RENbO$_4$ microwave dielectric ceramics have become ideal materials for preparing high-performance substrates, filters, and dielectric antennas.

In this paper, the entropy, as a regulation variable, was introduced into the preparation and property exploration of the RENbO$_4$ ceramics. Based on S_c, medium-entropy (with three or four rare-earth elements in the RE-site) and high-entropy (with five rare-earth elements in the RE-site) microwave dielectric ceramics were designed. In comparison with the low-entropy RENbO$_4$ ceramics (with solely one RE element), the effects of the entropy on crystal structure, microstructure, phase transition, and microwave dielectric properties were systematically studied. This work provides a

paradigm for the adjustment of the microwave dielectric properties via entropy engineering.

2   Experimental

Chemical formulae were recorded as $(La_{1/3}Nd_{1/3}Sm_{1/3})NbO_4$ (3RNO; $S_c = 1.10R$), $(La_{1/4}Nd_{1/4}Sm_{1/4}Ho_{1/4})NbO_4$ (4RNO; $S_c = 1.39R$), and $(La_{1/5}Nd_{1/5}Sm_{1/5}Ho_{1/5}Y_{1/5})NbO_4$ (5RNO; $S_c = 1.61R$), with the rare-earth elements in equal molar ratios. A solid-state reaction route was adopted to fabricate the ceramics from high-purity oxides (La_2O_3, Nd_2O_3, Sm_2O_3, Ho_2O_3, Y_2O_3, and Nb_2O_5; purity $\geqslant$ 99.9%, Aladdin). Firstly, raw materials were weighed and ball-milled for 6 h using alcohol as a milling medium. The fully mixed powders were calcined at 1250 ℃ for 8 h, followed by a second ball-milling for 6 h to obtain fine powders. An appropriate amount of 5 wt% polyvinyl alcohol (PVA) aqueous solution as a binder was added. The powders were pressed into cylindrical samples (10 mm in diameter and 5–6 mm in height) with a pressure of 70 MPa. To remove the PVA, the ceramic samples were kept at 550 ℃ for 6 h. Finally, the ceramics were sintered at 1210–1290 ℃ for 4 h.

Phase purity and crystal structure were analyzed by an X-ray diffractometer (Empyrean, PANalytical, the Netherlands). Microstructures and element distribution were observed by a scanning electron microscope (SEM; S-4800, Hitachi High-Technologies, Japan). In addition, a high-resolution transmission electron microscope (HRTEM; JEM-2100F, JEOL, Japan) and selected-area electron diffraction (SAED) pattern provide rich lattice information. Local structural features and intrinsic dielectric properties were analyzed by a Raman spectrometer (Fisher DXR, Thermo Electron, USA) and a far-infrared reflectivity (FIR) spectrometer (IFS 66v FT-IR, Bruker, Germany). Bulk densities of the ceramics were measured by Archimedes method. Identification of the phase transformation at different temperatures was characterized by variable-temperature X-ray diffraction (XRD), thermal expansion tester (PCY, Xiangtan Xiangyi Instrument, China), and electrochemical workstation (VSP, Bio-Logic, France). Finally, the microwave dielectric properties were tested by a vector network analyzer (Keysight E5071C, Keysight Technologies, USA) in TE_{011} mode using Hakki–Coleman dielectric resonator method [26]. The τ_f is calculated by Eq. (2) [27]:

$$\tau_f = \frac{1}{f_{25}} \cdot \frac{f_{85} - f_{25}}{85 - 25} \qquad (2)$$

where f_{85} and f_{25} correspond to the resonant frequencies at 85 and 25 ℃, respectively.

3   Results and discussion

3. 1   Preparation of 5RNO high-entropy ceramics

An XRD pattern of the mixed powders is shown in Fig. 1(a). By comparing, all the raw oxides including La_2O_3, Nd_2O_3, Sm_2O_3, Ho_2O_3, Y_2O_3, and Nb_2O_5 can be detected, which indicates the uniform mixing of precursors. After being fired at 1270 ℃ for 4 h, single-phase $(La,Nd,Sm,Ho,Y)NbO_4$ was achieved by indexing with the standard PDF cards, as shown in Fig. 1(b). One point should be noted that the XRD pattern of $(La,Nd,Sm,Ho,Y)NbO_4$ is similar to those of $RENbO_4$ (RE = La, Nd, Sm, Ho, and Y); however, a slight deviation in the position of XRD peaks is evident. This is because the average ionic radius in the RE-site for $(La,Nd,Sm,Ho,Y)NbO_4$ (~1.076 Å, coordination number (CN) = 8) is different from that of each of $RENbO_4$ (RE = La, Nd, Sm, Ho, and Y) individually [28]. These results manifest solid solution of the five rare-earth elements (La, Nd, Sm, Ho, and Y) into the RE-site and formation of the high-entropy ceramics. Rietveld refinement provides evidence for the phase purity and cation occupation in the targeted 5RNO. As shown in Fig. 1(c), the observed and calculated patterns match well, and the Rietveld reliability factor (R_{wp}) value and the goodness of fit (GOF) are lower than 10% (R_{wp} = 5.62%, GOF = 3.13), indicating that the result is reliable [29]. The high-entropy $RENbO_4$ ceramics exhibit a single-phase fergusonite structure with the monoclinic space group ($C2/c$). The crystal structure of the title 5RNO is shown in Fig. 1(d), with La^{3+}, Nd^{3+}, Sm^{3+}, Ho^{3+}, and Y^{3+} occupying the RE-site equally and randomly [30]. It consists of $[NbO_4]$ tetrahedra and $[ReO_8]$ decahedra. The adjacent $[ReO_8]$ decahedra units form chains by sharing edges, while $[NbO_4]$ and $[ReO_8]$ are corner-connected by sharing oxygen ions.

Microscopic morphology and element distribution of a grain surface further confirm the formation of high-entropy solid solution. As shown in Fig. 2, the SEM image revealed a dense microstructure, characterized by closely packed grains with clear grain boundaries and no visible pores. The grain size is in the range of
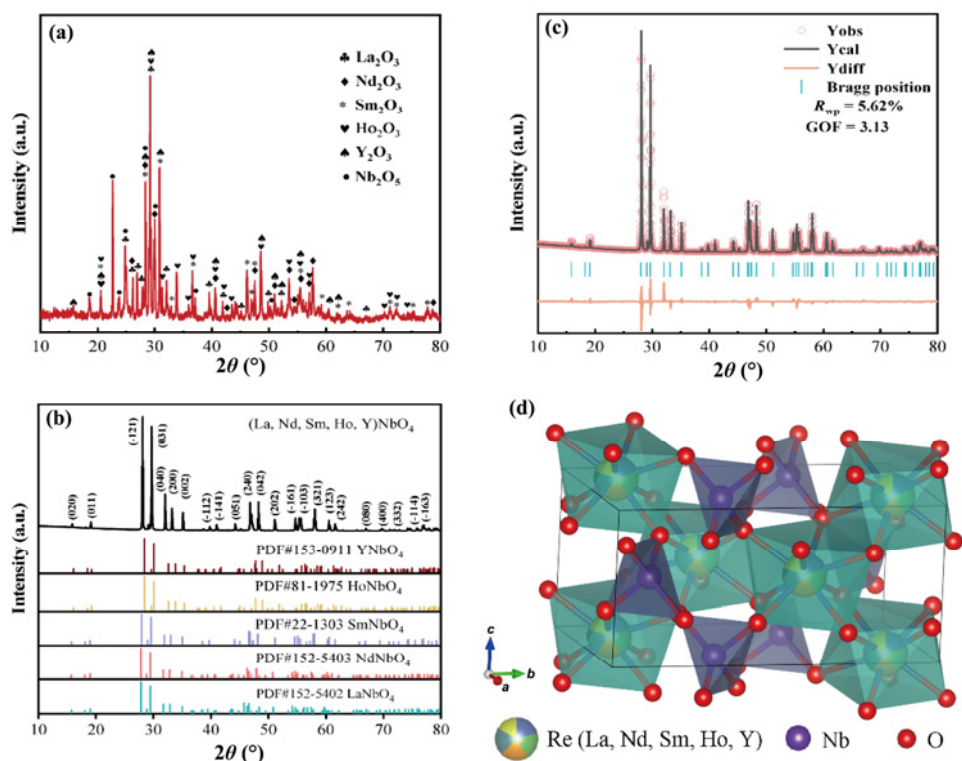
清华大学出版社 | Sci●pen
Tsinghua University Press

Fig. 1 (a) XRD pattern of mixed powders (XRD peaks are the superposition of six raw materials); (b) XRD pattern of 5RNO high-entropy ceramics sintered at 1270 ℃ (XRD peak assignment was performed); (c) Rietveld refinement of powder XRD patterns of 5RNO high-entropy ceramics sintered at 1270 ℃ (R_{wp} = 5.62%, GOF = 3.13) wherein Yobs, Ycal, and Ydiff represent the observe, calculate, and difference intensity respectively; (d) crystal structure of 5RNO high-entropy ceramics, which consists of [NbO$_4$] tetrahedra and [ReO$_8$] decahedra.
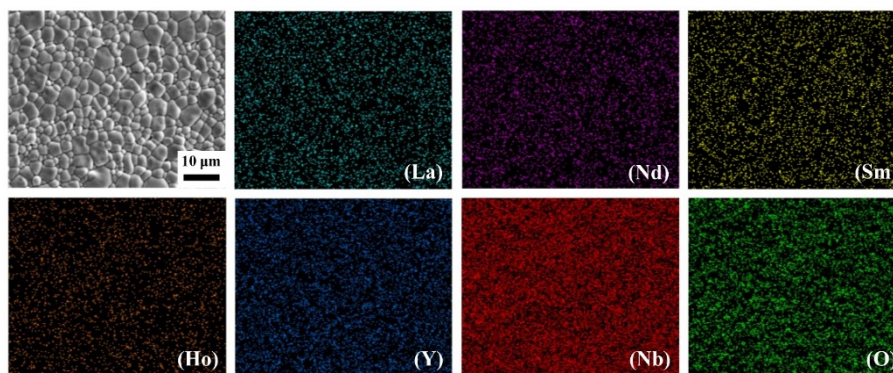

Fig. 2 SEM–EDS mappings of 5RNO high-entropy ceramics; points of different colors represent uniformly distributed La, Nd, Sm, Ho, Y, Nb, and O.

1–4 μm. All rare-earth elements were distributed uniformly. Figure 3(a) shows an SAED pattern along the [021] zone axis, which can be indexed as the monoclinic fergusonite with (200), (2−12), and (0−12) fundamental reflections. The HRTEM micrograph of 5RNO (Fig. 3(b)) displays an interplanar spacing in the particle projected along [020]. They matched well with the monoclinic fergusonite model (space group: *C*2/*c*). By TEM–energy dispersive spectroscopy (EDS)

(Fig. 3(c)), the element distributions on the nanoscale are also uniform, which correspond to the SEM–EDS. All the results show that the monoclinic 5RNO was successfully synthesized.

3. 2 Effects of entropy (3RNO, 4RNO, and 5RNO) on structure and microstructure

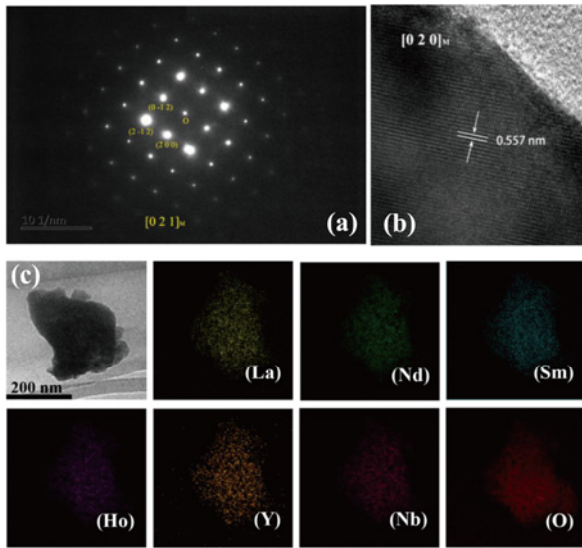To reveal the effects of the entropy on the structure of RENbO$_4$, two medium-entropy ceramics, (La,Nd,Sm)NbO$_4$

Fig. 3 (a) SAED pattern of monoclinic 5RNO taken along [021] zone axis; (b) HRTEM micrograph of 5RNO projected along [020]; (c) TEM–EDS mappings of 5RNO (the points of different colors represent uniformly distributed La, Nd, Sm, Ho, Y, Nb, and O).

(abbreviated as 3RNO and 4RNO, respecively), were designed and fabricated at 1270 ℃ and 4 h for comparison. Similar to the title 5RNO counterpart, both medium-entropy ceramics crystallized in a single fergusonite structure (Figs. 4(a) and 4(b)), which uncovers the entropy-dominated phase stabilization. Figure 4(c) compares the XRD profiles of the 3RNO (S_c = 1.10R), 4RNO (S_c = 1.39R), and 5RNO (S_c = 1.61R) ceramics. The enlarged diffraction peaks at around $2\theta = 28°$ exhibit a distinct peak shift to high angles with the increasing configurational entropy. The average RE-site radii of the 3RNO, 4RNO, and 5RNO compounds is 1.116, 1.091, and 1.076 Å, respectively, which are responsible for the high-angle peak shift. These results indicate that it is feasible to regulate the structure by the entropy. The R_{wp} values (GOF) and parts of refinement crystal structure data of 3RNO, 4RNO, and 5RNO are shown in Table 1. The structural characterizations by Rietveld refinement are shown in Table 2.
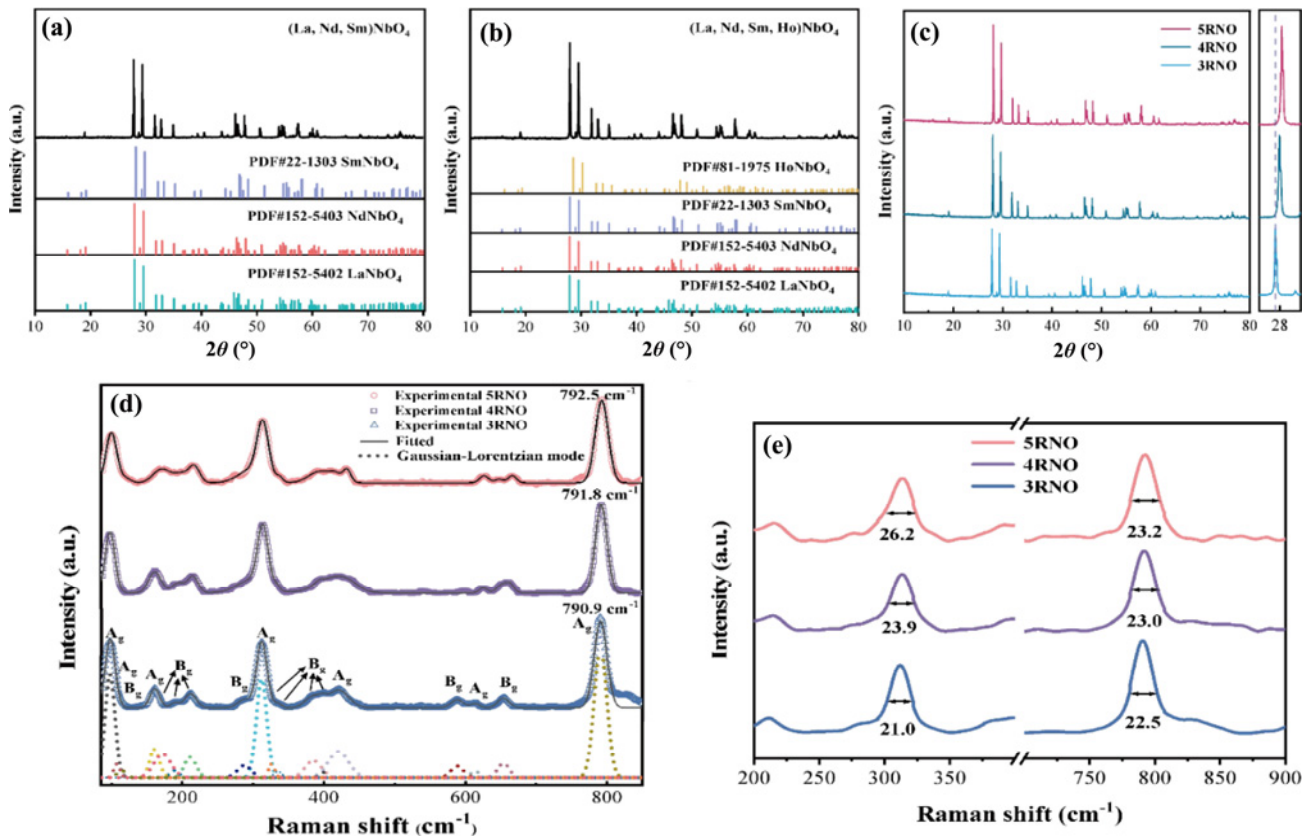

Fig. 4 (a) XRD pattern of 3RNO medium-entropy ceramics sintered at 1270 ℃; (b) XRD pattern of 4RNO medium-entropy ceramics sintered at 1270 ℃; (c) XRD patterns of RENbO$_4$ samples sintered at 1270 ℃ and enlarged diffraction patterns in region of $2\theta = 27°$–29°; (d) room-temperature Raman spectra of 3RNO, 4RNO, and 5RNO (the dashed lines indicate Gaussian–Lorentzian mode fit); (e) amplified Raman spectra at 310 and 790 cm^{-1} and their full widths at half maximum (FWHMs).

Table 1 Crystallographic information of 3RNO, 4RNO, and 5RNO ceramics sintered at 1270 ℃

Composition	a (Å)	b (Å)	c (Å)	V_{cell} (Å^3)	R_{wp} (%)	GOF	ρ_{th} (g/cm^3)
3RNO	5.4788(0)	11.3135(7)	5.1513(1)	318.3573(1)	10.1(0)	5.8(9)	6.26
4RNO	5.4387(3)	11.2370(3)	5.1385(8)	313.1136(3)	4.5(1)	2.5(6)	6.51
5RNO	5.4125(3)	11.1855(7)	5.1283(3)	309.5589(2)	5.6(2)	3.1(3)	6.32

Note: a, b, and c represent the lattice parameters, V_{cell} represents the volume of the unit, and ρ_{th} is the theoretical density.

Table 2 Structural characterizations of 3RNO, 4RNO, and 5RNO ceramics

Composition	Element	Wyckoff site	x	y	z	Biso.
3RNO	RE	4e	0.00000	0.62930	0.25000	0.8351
	Nb	4e	0.00000	0.10390	0.25000	1.6853
	O1	8f	0.23980	0.03230	0.04460	0.3764
	O2	8f	0.15150	0.20680	0.49060	0.9527
4RNO	RE	4e	0.25000	0.12078	0.00000	0.6845
	Nb	4e	0.25000	0.64619	0.00000	1.8592
	O1	8f	0.00760	0.71551	0.20290	0.4369
	O2	8f	0.90390	0.45567	0.24630	0.8142
5RNO	RE	4e	0.25000	0.12078	0.00000	0.7642
	Nb	4e	0.25000	0.64619	0.00000	1.7631
	O1	8f	0.00760	0.71551	0.20290	0.4527
	O2	8f	0.90390	0.45567	0.24630	0.8147

Note: Biso. is the isotropic temperature factor.

Similar to the XRD pattern, Raman scattering spectrum is the "fingerprint" of the phase but is more sensitive to the local structural evolution [31]. The effective radii of different rare-earth ions affect the distortion of the [ReO$_8$] oxygen decahedral, and the slight change of the [ReO$_8$] oxygen decahedral will make the [NbO$_4$] oxygen tetrahedra be implicated, resulting in the corresponding change of vibration of a chemical bond, which is reflected in the subtle change of Raman vibration peak. Figure 4(d) shows Raman scattering spectra of 3RNO, 4RNO, and 5RNO samples. According to lattice point group predication, there are 18 Raman active modes in a RENbO$_4$ monoclinic structure, and the Γ point of Brillouin zone can be expressed by Eq. (3) [29,32]:

$$\Gamma = 8A_g + 10B_g \tag{3}$$

Raman modes near 310 and 790 cm^{-1} represent symmetric stretching vibration of the Nb–O bond in the [NbO$_4$] oxygen tetrahedron [33,34]. As shown in Fig. 4(d), 18 peaks matched well with Raman mode of RENbO$_4$, and the phase can be distinguished by these Raman modes. Raman peaks at 310 and 790 cm^{-1} shift to the high frequency side with an increase in the entropy, which is due to the contraction of the [ReO$_8$] oxygen decahedral and the enhancement of bond

strength because of a decrease in the effective rare-earth ion radius [35,36]. The amplified Raman peaks near 310 and 790 cm^{-1} and their FWHMs by peak fitting are shown in Fig. 4(e); the FWHMs of Raman peak near 310 and 790 cm^{-1} enlarged with an increase in S_c, which was attributed to an increase in disorder degree [37–39]. Through the above verification, the single-phase RENbO$_4$ ceramics can be entropy stabilized, and the local structure strongly correlates with the radius of rare-earth cations.

Microscopic SEM images of the 3RNO, 4RNO, and 5RNO ceramics sintered at 1270 ℃ are shown in Figs. 5(a)–5(c). It can be intuitively observed that the grains of all ceramics are well-developed, and grain boundaries are clear, showing a dense microstructure. The average grain sizes of the 3RNO, 4RNO, and 5RNO ceramics are 3.6, 3.0, and 3.2 μm, respectively. Figure 5(d) shows a variation trend of the density of each ceramic sample at different sintering temperatures. Strong dependence on the sintering temperature (S.T.) of the density is observed for the three samples. Similarly, increasing the sintering temperature improves the density of the ceramics, which is due to the high sintering temperature promoting the grain growth and uniform grain distribution. All three components can be densified at 1270 ℃ with the highest density. The
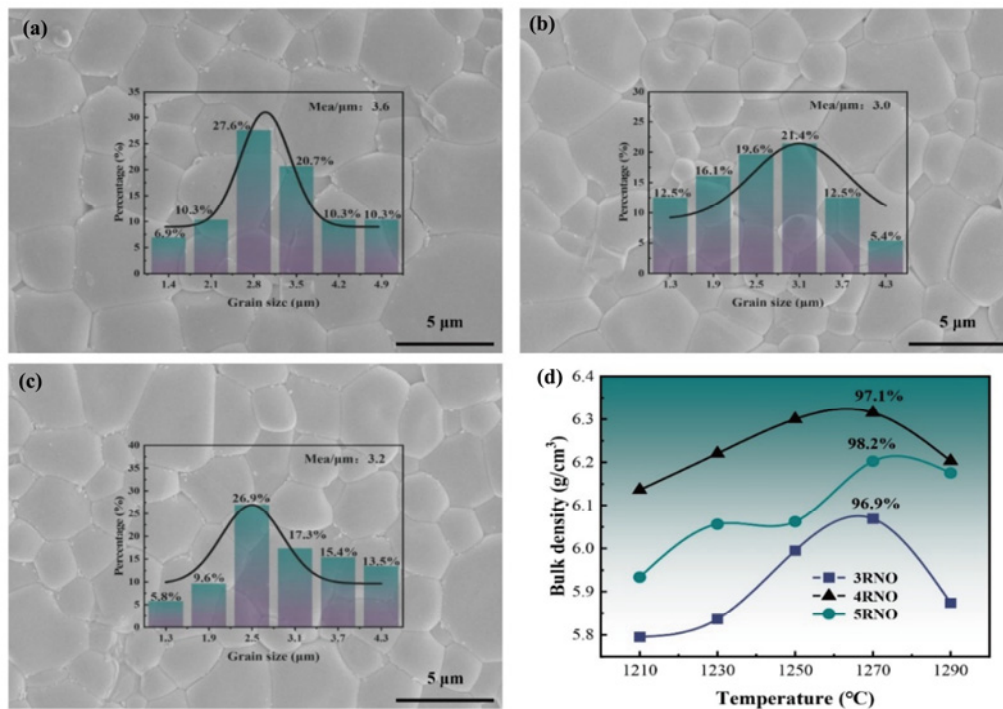
Fig. 5 SEM images of (a) 3RNO, (b) 4RNO, and (c) 5RNO ceramics by being fired at 1270 ℃ for 4 h (grain size distributions have been shown in them, normal distribution is used as a function to fit grain size distribution, and fitting is good); (d) bulk densities at different sintering temperatures (the highest densities have been marked).

relative density of each component has been highlighted (Fig. 5(d)), all of which are larger than 95%. In addition, the bulk density of the 4RNO ceramics is higher than those of the 3RNO and 5RNO ceramics owing to the difference in their ρ_{th}. The ρ_{th} could be defined by Eq. (4) [40]:

$$\rho_{th} = \frac{MN}{N_A V_{cell}} \tag{4}$$

where M is the atom weight, N is the number of atoms in the unit, and N_A is the Avogadro's number. As shown in Table 1, ρ_{th} of 4RNO is calculated as 6.51 g/cm^3, which is much higher than those of the 3RNO (6.26 g/cm^3) and 5RNO ceramics (6.32 g/cm^3). The maximum experimental density of the 4RNO ceramics is 6.32 g/cm^3 with a relative density of 97.1%.

3.3 High-entropy effect on phase transition of LaNbO$_4$

LaNbO$_4$ has been reported to undergo a reversible phase transition at around 540 ℃ from high-temperature scheelite (tetragonal, $I4_1/a$) to fergusonite-type (monoclinic, $C2/c$) structure [23,41]. Of particular importance is the effect of high entropy on the phase transition behavior of LaNbO$_4$ to understand the stable operating temperature range.

The *in-situ* XRD measurements were carried out for 5RNO at variable temperatures (100–720 ℃) to determine the phase transition temperature. As shown in Fig. 6(a), low-temperature XRD patterns match well with monoclinic fergusonite-type LaNbO$_4$ (PDF Card No. 152-5402), as characterized by the split (021) and (−221) peaks. With the increasing temperature, the split peaks gradually approached and merged into one (112) peak at around 700 ℃, as a characteristic diffraction peak for the tetragonal scheelite phase (PDF Card No. 153-6267). This result indicates that the phase transition from fergusonite to scheelite occurred at 700 ℃. The *a*, *b*, and *c* calculated by the least squares method [42] are shown in Fig. 6(b). Obviously, before the phase transition, *a* decreases with the increasing temperature, while both *b* and *c* increase. When reaching the phase transition temperature, the crystal changes from monoclinic to tetragonal, and $a = c$ is a typical feature of tetragonal [43,44]. Compared with that of the pure LaNbO$_4$ phase, the phase transition temperature is increased by 30% (~160 ℃). Such large difference is ascribed to be due to the size effect of the rare-earth elements on the phase transition temperature. It has been established that the larger the RE element, the lower the phase transition temperature of RENbO$_4$ is [45,46].
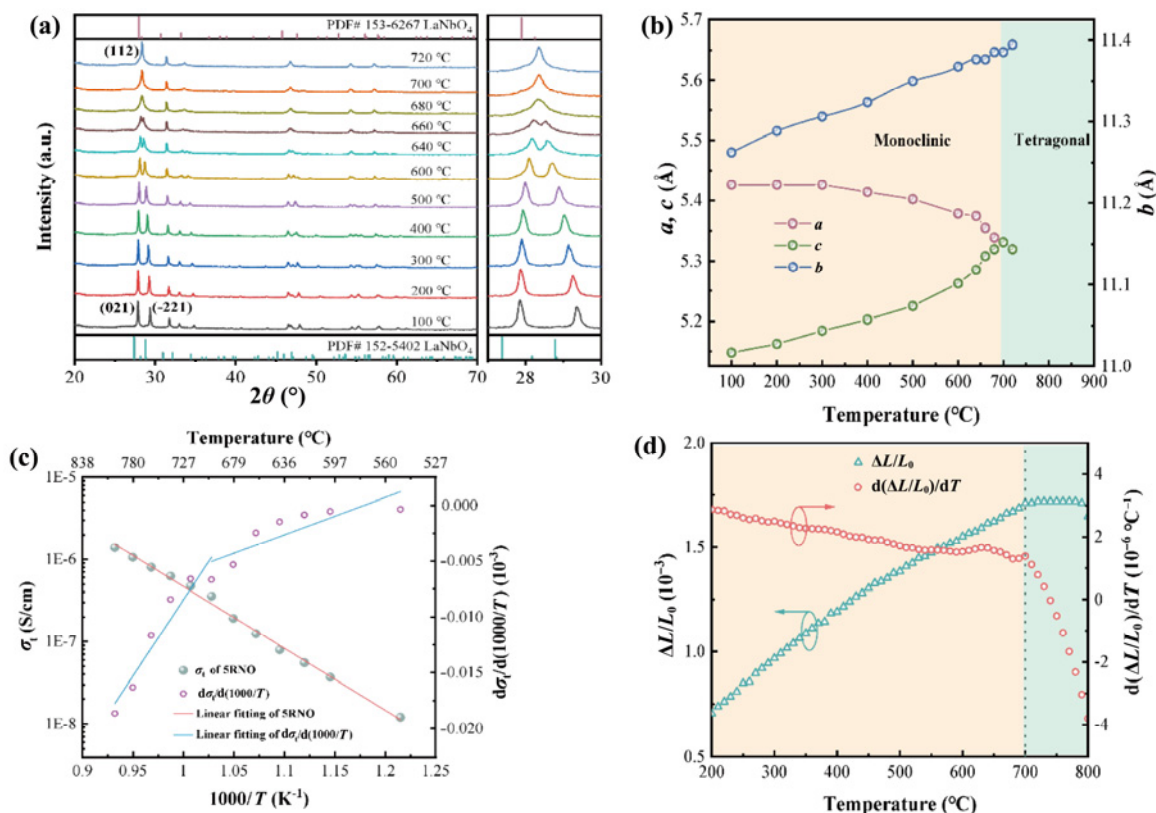
Fig. 6 (a) XRD patterns of 5RNO at 100–720 ℃ (the change of XRD peak indicates that monoclinic–tetragonal phase transition occurs); (b) *a*, *b*, and *c* of 5RNO at 100–720 ℃; (c) conductivity (σ_t) and its variation coefficients (dσ/d*T*) of 5RNO at 550–800 ℃; (d) thermal expansion change rates ($\Delta L/L_0$) and thermal expansion coefficients (d($\Delta L/L_0$)/d*T*) of 5RNO at 200–800 ℃.

The alternating current (AC) conductivity and thermal expansion measurements provide robust evidence for the observed phase transition. If a solid electrolyte is stable in the temperature range, its σ_t shows a uniform and regular linear change [47–49]. Figure 6(c) shows a σ_t curve and dσ/d*T* change of 5RNO at 550–800 ℃. Discontinuous changes in dσ/d*T* can be observed with a breakpoint at 700 ℃. Similarly, it can be found in Fig. 6(d) that $\Delta L/L_0$ and d($\Delta L/L_0$)/d*T* have a discontinuous trend at 700 ℃, which was due to the change of the structure caused by the phase transformation, resulting in the difference of a expansion rate [50].

3.4 High-entropy effect on microwave dielectric properties

Figure 7(a) shows a change in the dielectric permittivity (ε_r) of three RNO ceramics as a function of the sintering temperature. The ε_r of all ceramic samples is between 18 and 20, and first increases with the

sintering temperature, and then decreases when the sintering temperature is higher than 1270 ℃. The dielectric permittivity and bulk density experience the same variation trend, which verifies that the density is an important factor affecting ε_r. The variation in the $Q{\times}f$ values (Fig. 7(b)) of the 3RNO, 4RNO, and 5RNO ceramics exhibits a similar tendency and reaches their respectively optimal values at 1270 ℃, indicating that rising the density is beneficial to improving the $Q{\times}f$ values.

The optimal microwave dielectric properties of each composition are summarized in Table 3. By comparison, ε_r increases from 19.13 for 3RNO to 19.22 for 4RNO, and to 19.48 for 5RNO. As established by Clausius–Mosotti (C–M) equation, ε_r is closely related to the molar volume (V_m) and the molecular polarizability (α), and the theoretical dielectric permittivity ($\varepsilon_{th.}$) can be expressed by Eq. (5) [51]:

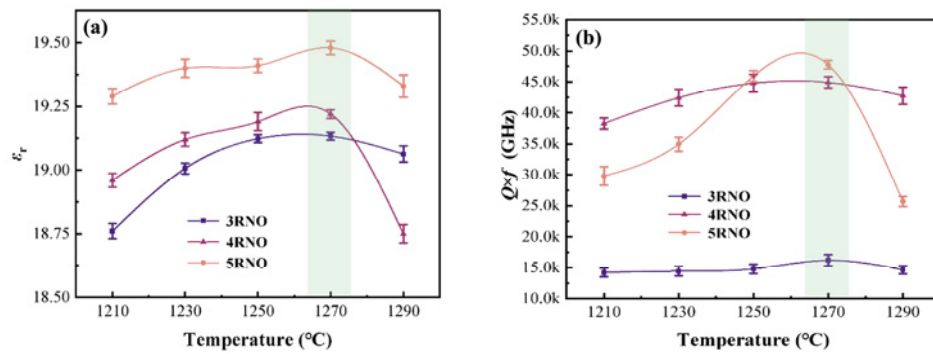$$\varepsilon_{th.} = \frac{3V_m + 8}{3V_m - 4} \tag{5}$$

Fig. 7 (a) ε_r and (b) $Q \times f$ of 3RNO, 4RNO, and 5RNO ceramics by sintering at different temperatures. Error data have been added to dielectric properties.

Table 3 Microwave dielectric properties, polarizability of unit volume, packing fractions (PFs), and bond valences of RNO ceramics

Composition	S.T. (℃)	ε_r	$Q \times f$ (GHz)	τ_f (ppm/℃)	α (Å³)	α/V_m	PF (%)	V_{Nb-O}
3RNO	1270	19.13	16,190	1.75(3)	17.2833	0.2102	60.85	4.2714
4RNO	1270	19.22	44,920	−5.87(7)	16.9575	0.2166	61.38	4.3248
5RNO	1270	19.48	47,770	−13.50(2)	16.7300	0.2233	61.81	4.4058

Note: V_{Nb-O} is the valence of the Nb–O bond.

Additionally, taking the variable (α/V_m) as a whole, a directly proportional correlation can be established between the permittivity and the α/V_m term [52]. As listed in Table 3, the increasing α/V_m from 3RNO (0.2102) to 5RNO (0.2233) is responsible for the rising permittivity. Similarly, a steady increase in $Q \times f$ is observed from 16,190 GHz for 3RNO to 44,920 and 47,770 GHz for 4RNO and 5RNO, respectively.

Kim *et al.* [53] found that $Q \times f$ was strongly correlated with the PF in ABO₄ ceramics, and $Q \times f$ increased with the PF. This is because the decrease of the lattice vibration space resulting from the increasing PF leads to a decrease in tanδ [54]. Subsequently, the PF rule has been verified in some microwave dielectric ceramics [55–57]. The PF could be obtained by Eq. (6) [58]:

$$\text{PF (\%)} = \frac{\text{Volume of packed ions}}{\text{Volume of primitive unit cell}}$$
$$= \frac{\text{Volume of packed ions}}{\text{Volume of unit cell}} \times Z \tag{6}$$

where Z is the number of formula units per unit cell. As listed in Table 3, the increase in $Q \times f$ from the 3RNO (16,190 GHz) to the 5RNO (47,770 GHz) ceramics with the increasing PF verifies the primary influence of the PF.

Bond valence theory is an important method to predict the τ_f value of the microwave dielectric ceramics [53]. The bond valence of atom i (V_i) can be defined as the sum of all the valences (v_{ij}) from a given atom i, and the bond valence can be calculated by Eqs. (7) and (8) [59]:

$$V_i = \sum_j v_{ij} \tag{7}$$

$$v_{ij} = \exp\left(\frac{R_{ij} - d_{ij}}{b}\right) \tag{8}$$

where R_{ij} is the bond valence parameter [60], d_{ij} is the bond length of atoms i and j, and b is the universal constant equal to 0.37 Å. As Kim *et al.* [53] found that with the increase in the bond strength, recovery force of polyhedron tilt increases, and τ_f would decrease. The τ_f and V_{Nb-O} of 3RNO, 4RNO, and 5RNO are shown in Table 3. When S_c of the system increases, V_{Nb-O} increases from 4.2714 to 4.4058, and the τ_f value decreases from a positive value of 1.75 ppm/℃ for 3RNO to −5.87 ppm/℃ for 4RNO and −13.50 ppm/℃ for 5RNO.

The FIR spectroscopy analyzes the intrinsic dielectric properties by correlating the lattice vibration [61]. To further study the intrinsic microwave dielectric properties of the 3RNO, 4RNO, and 5RNO ceramics, the intrinsic dielectric permittivity and loss were fitted by Kramers–Kronig (K–K) equation. It can be expressed by Eqs. (9) and (10) [62]:

$$\varepsilon' = \varepsilon_\infty + \sum_{j=1}^{n} \frac{\omega_{pj}^2}{\omega_{0j}^2} = \varepsilon_\infty + \sum_{j=1}^{n} \varepsilon_j \tag{9}$$

$$\tan \delta(\omega) = \frac{\varepsilon''}{\varepsilon'} = \omega \sum_{j=1}^{n} \frac{\varepsilon_j \gamma_j}{\omega_{0j}^2 \left(\varepsilon_\infty + \sum_{j=1}^{n} \varepsilon_j \right)} \qquad (10)$$

where ε' and ε'' are the real and imaginary parts of the dielectric permittivity, respectively, ω is the test frequency, ω_{0j}, ω_{pj}, and γ_j are the transverse frequency, the plasma frequency, and the damping coefficient of the j-th FIR mode, respectively, and ε_∞ and $\Delta\varepsilon_j$ are the dielectric permittivity contribution of the electronic polarization and the j-th FIR mode to the dielectric permittivity, respectively. Therefore, the fitted theoretical dielectric permittivity is $\varepsilon_r = \varepsilon_\infty + \Sigma\Delta\varepsilon_j$.

All far-infrared spectra can be fitted by Eqs. (9) and (10), and the fitting results are good, as shown in Figs. 8(a)–8(d). The related phonon parameters of the 3RNO, 4RNO, and 5RNO ceramics are shown in Table 4, indicating that the ceramics have 14 far-infrared modes. The static dielectric permittivity ($\Sigma\Delta\varepsilon_j$) is very close to those of the TE_{011} measured values, and ε_∞ is small (from 1.72 to 2.61). The results show that the dielectric response mainly comes from the oscillation absorption of phonons at microwave

frequencies. In addition, there is a large difference between the measured and theoretical values of ε''. The measured value of ε'' is lower than the theoretical one, and it is unreasonable. This may be explained by that the predicted $\tan\delta$ at microwave frequencies from infrared reflection spectra is lack accuracy (Table 5). This is because there are still some differences in ceramic performance in optical and microwave frequency regions.

Figure 9 compares the microwave dielectric properties of the present entropy-stabilized RNO ceramics with the RENbO$_4$ counterparts with merely one rare-earth element in the RE-site. No distinct difference in ε_r is shown, and the ε_r values for RENbO$_4$ are around 20 except for YNbO$_4$. On the contrary, $Q\times f$ of 3RNO is much lower than those of discrete RENbO$_4$ (e.g., 54,400 GHz for LaNbO$_4$, 33,000 GHz for NdNbO$_4$, and 56,300 GHz for SmNbO$_4$), whereas the 4RNO and 5RNO counterparts exhibit a slightly lower but comparable $Q\times f$. The discrepancy in $Q\times f$ is believed to stem from competitive effects of cation disorder induced by increasing the entropy and PF. Of particular significance is the
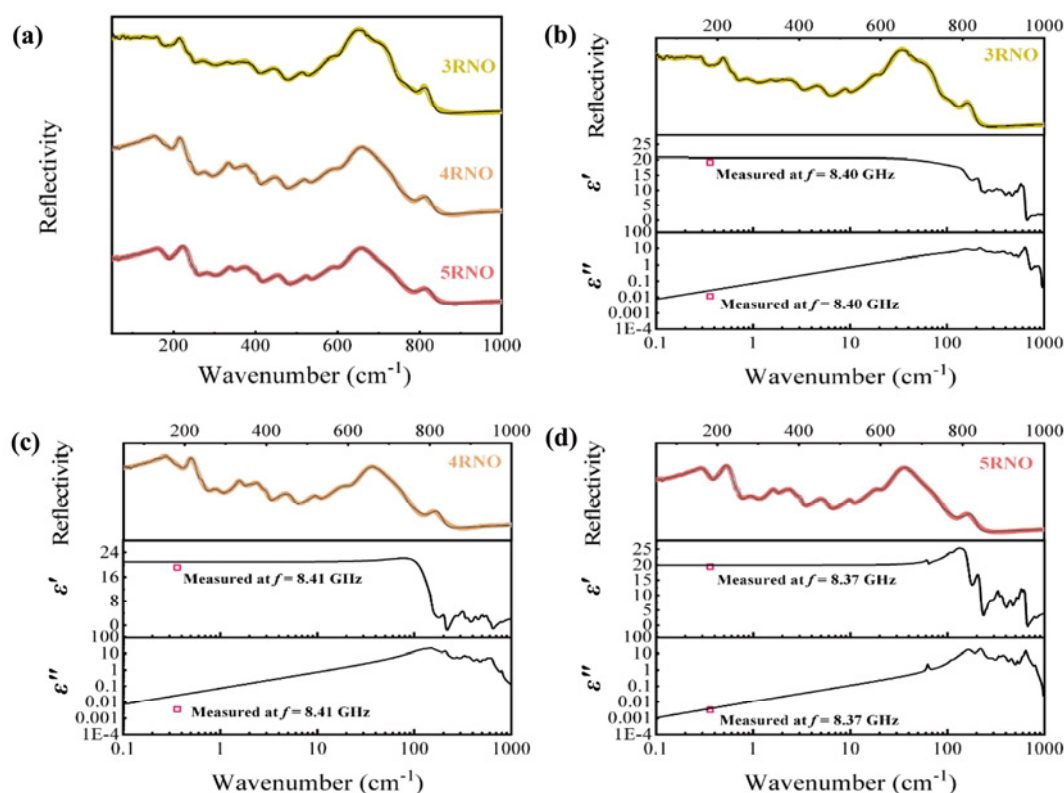

Fig. 8 (a) Experimental and fitted infrared reflection spectra (the solid lines for fitted and the dotted lines for experimental) of 3RNO, 4RNO, and 5RNO ceramics. Fitted complex dielectric spectra of (b) 3RNO, (c) 4RNO, and (d) 5RNO ceramics (the squares represent the measured values in TE_{011} mode).

Table 4   Phonon parameters obtained by fitting FIR of 3RNO, 4RNO, and 5RNO ceramics

Mode	3RNO				4RNO				5RNO			
	ω_{oj}	ω_{pj}	γ_j	$\Delta\varepsilon_j$	ω_{oj}	ω_{pj}	γ_j	$\Delta\varepsilon_j$	ω_{oj}	ω_{pj}	γ_j	$\Delta\varepsilon_j$
1	163.11	44.65	11.28	0.5916	149.93	134.17	24.16	1.4865	109.87	30.99	12.24	1.1222
2	166.34	310.22	127.72	6.5758	152.93	642.54	114.05	6.8876	139.36	135.76	43.49	3.1542
3	219.48	157.46	28.54	1.1131	210.28	201.7	20.51	0.9002	166.48	314.49	41.33	2.5072
4	240.86	74.881	19.558	0.6953	276.08	129.88	29.605	0.9879	220.38	360.03	34.97	1.6074
5	279.08	170.27	57.02	1.7467	331.51	106.86	15.94	0.4441	285.7	217.42	53.93	1.9107
6	338.98	202.77	74.92	1.8923	332.61	319.48	65.572	1.8189	338.45	164.62	23.08	0.6895
7	386.3	235.72	59.13	1.3100	372.56	279.66	45.1	1.1172	377.27	369.4	55.06	1.4760
8	452.9	210.86	47.75	0.8990	396.11	55.42	10.09	0.2354	401.93	74.1	13.07	0.3286
9	516.39	102.21	21.96	0.3639	445.76	280.53	48.51	1.0064	458.01	259.03	40.36	0.8907
10	586.87	110.29	21.05	0.3074	516.41	224.23	39.85	0.7128	526.66	137.41	18.94	0.3639
11	647.76	556.73	62.68	0.8288	581.46	441.66	68.2	1.0802	589.78	236.9	31.187	0.5348
12	699.82	410.07	75.74	0.9247	636.08	564.35	61.09	0.8863	641.42	662.25	52.38	0.8260
13	771.04	152.55	45.55	0.5060	698.91	223.85	102.62	1.3572	698.14	456.09	141.98	2.0523
14	809.5	166.98	30.75	0.3254	803.66	169.16	37.34	0.4293	805.17	194.16	43.098	0.5409
	$\varepsilon_\infty = 2.61$		$\Sigma\Delta\varepsilon_j = 18.08$		$\varepsilon_\infty = 1.72$		$\Sigma\Delta\varepsilon_j = 19.35$		$\varepsilon_\infty = 1.96$		$\Sigma\Delta\varepsilon_j = 18.00$	

Table 5   Measured and calculated values of ε' and ε'' at 8.40 GHz of 3RNO, 4RNO, and 5RNO ceramics

System	Measured		Calculated	
	ε'	ε''	ε'	ε''
3RNO	19.13	0.0113	20.69	0.0263
4RNO	19.22	0.0035	21.07	0.0260
5RNO	19.48	0.0033	19.96	0.0040

Note: ε' and ε'' represent the real and imaginary numbers of complex dielectric permittivity.
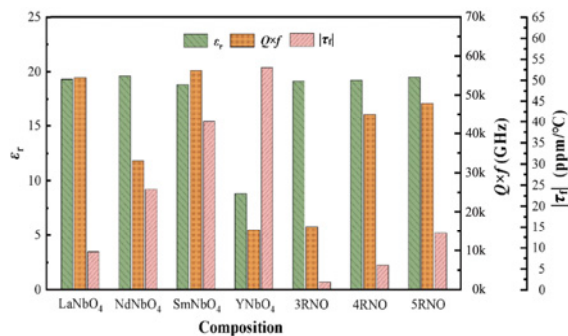

Fig. 9   Comparison of microwave dielectric properties of RENbO$_4$.

near-zero τ_f value of entropy stabilized RNO ceramics, especially for the 3RNO and 4RNO samples, which is different from that of LaNbO$_4$ (~9 ppm/℃), NdNbO$_4$ (~−24 ppm/℃), SmNbO$_4$ (~−40 ppm/℃), and YNbO$_4$ (~−53 ppm/℃) [24,25]. However, when they are solid solution in an equal proportion, they are more likely to get a large negative τ_f value. It can be inferred that near-zero temperature coefficient of the resonant

frequency of the microwave dielectric ceramics might be related to the multi-ion synergy generated by the entropy effect, which opens an avenue for material exploration and property optimization via entropy engineering. Thus, the high-entropy microwave dielectric ceramics are expected to become potential materials for practical applications.

4   Conclusions

In this study, RENbO$_4$ medium-entropy (3RNO and 4RNO) and high-entropy (5RNO) microwave dielectric ceramics were prepared via the solid-phase method. All ceramics were monoclinic fergusonite structured with the space group of $C2/c$. The crystal structures, phase transitions, microscopic morphologies, vibration characteristics, and bond valences of the RENbO$_4$ ceramics were analyzed by the XRD, SEM–EDS, Raman spectra, and far-infrared spectra, and the dielectric properties were explained by the C–M equation, PF, and bond valence theory. It was found that the ceramics sintered at 1270 ℃ had the best performance. The 3RNO sample has the most stable τ_f (≈ 1.75 ppm/℃), and the 5RNO sample obtains the highest $Q \times f$ (≈ 47,770 GHz), while the 4RNO sample exhibits the optimal overall performance with ε_r = 19.22, $Q \times f$ = 44,920 GHz, and τ_f = −5.87 ppm/℃. This work opens an avenue for novel material exploration

and property optimization via entropy engineering. From a viewpoint of material design, the entropy engineering may result in synergetic optimization of the dielectric properties in the microwave materials. This may help guide future material design to meet the requirements of different dielectric applications.

Acknowledgements

References

[1] Li CC, Yin CZ, Khaliq J, *et al*. Ultralow-temperature synthesis and densification of $Ag_2CaV_4O_{12}$ with improved microwave dielectric performances. *ACS Sustainable Chem Eng* 2021, **9**: 14461–14469.

[2] Xiong Y, Xie HY, Rao ZG, *et al*. Compositional modulation in $ZnGa_2O_4$ via Zn^{2+}/Ge^{4+} co-doping to simultaneously lower sintering temperature and improve microwave dielectric properties. *J Adv Ceram* 2021, **10**: 1360–1370.

[3] Zhang P, Zhao YG. Influence of Sm^{3+} substitutions for Nd^{3+} on the microwave dielectric properties of $(Nd_{1-x}Sm_x)NbO_4$ (x = 0.02–0.15) ceramics. *J Alloys Compd* 2016, **654**: 240–245.

[4] Feng C, Zhou X, Tao BJ, *et al*. Crystal structure and enhanced microwave dielectric properties of the $Ce_2[Zr_{1-x}(Al_{1/2}Ta_{1/2})_x]_3(MoO_4)_9$ ceramics at microwave frequency. *J Adv Ceram* 2022, **11**: 392–402.

[5] Wang DW, Zhang SY, Wang G, *et al*. Cold sintered $CaTiO_3$–K_2MoO_4 microwave dielectric ceramics for integrated microstrip patch antennas. *Appl Mater Today* 2020, **18**: 100519.

[6] Xiang HM, Xing Y, Dai FZ, *et al*. High-entropy ceramics: Present status, challenges, and a look forward. *J Adv Ceram* 2021, **10**: 385–441.

[7] Zhang LT, Duan YJ, Wada T, *et al*. Dynamic mechanical relaxation behavior of $Zr_{35}Hf_{17.5}Ti_{5.5}Al_{12.5}Co_{7.5}Ni_{12}Cu_{10}$ high entropy bulk metallic glass. *J Mater Sci Technol* 2021, **83**: 248–255.

[8] Li HY, Zhou Y, Liang ZH, *et al*. High-entropy oxides: Advanced research on electrical properties. *Coatings* 2021, **11**: 628.

[9] Chen J, Liu WX, Liu JX, *et al*. Stability and compressibility of cation-doped high-entropy oxide $MgCoNiCuZnO_5$. *J Phys Chem C* 2019, **123**: 17735–17744.

[10] Rost CM, Sachet E, Borman T, *et al*. Entropy-stabilized oxides. *Nat Commun* 2015, **6**: 8485.

[11] Chen H, Xiang HM, Dai FZ, *et al*. High porosity and low thermal conductivity high entropy $(Zr_{0.2}Hf_{0.2}Ti_{0.2}Nb_{0.2}Ta_{0.2})C$. *J Mater Sci Technol* 2019, **35**: 1700–1705.

[12] Zhang Z, Zhu SZ, Liu YB, *et al*. Enthalpy driving force and chemical bond weakening: The solid-solution formation mechanism and densification behavior of high-entropy diborides $(Hf_{1-x/4}Zr_{1-x/4}Nb_{1-x/4}Ta_{1-x/4}Sc_x)B_2$. *J Eur Ceram Soc* 2022, **42**: 3685–3698.

[13] Guo XT, Zhang YL, Li T, *et al*. High-entropy rare-earth disilicate $(Lu_{0.2}Yb_{0.2}Er_{0.2}Tm_{0.2}Sc_{0.2})_2Si_2O_7$: A potential environmental barrier coating material. *J Eur Ceram Soc* 2022, **42**: 3570–3578.

[14] Oses C, Toher C, Curtarolo S. High-entropy ceramics. *Nat Rev Mater* 2020, **5**: 295–309.

[15] Zhou SY, Pu YP, Zhang QW, *et al*. Microstructure and dielectric properties of high entropy $Ba(Zr_{0.2}Ti_{0.2}Sn_{0.2}Hf_{0.2}Me_{0.2})O_3$ perovskite oxides. *Ceram Int* 2020, **46**: 7430–7437.

[16] Xie HH, Li JS, Yang SZ, *et al*. Microstructures and dielectric properties of novel $(La_{0.2}Pr_{0.2}Nd_{0.2}Sm_{0.2}Eu_{0.2})_2Ce_2O_7$ high entropy ceramics. *J Mater Sci Mater Electron* 2021, **32**: 27860–27870.

[17] Xiang HC, Yao L, Chen JQ, *et al*. Microwave dielectric high-entropy ceramic $Li(Gd_{0.2}Ho_{0.2}Er_{0.2}Yb_{0.2}Lu_{0.2})GeO_4$ with stable temperature coefficient for low-temperature cofired ceramic technologies. *J Mater Sci Technol* 2021, **93**: 28–32.

[18] Liu K, Zhang HW, Liu C, *et al*. Crystal structure and microwave dielectric properties of $(Mg_{0.2}Ni_{0.2}Zn_{0.2}Co_{0.2}Mn_{0.2})_2SiO_4$—A novel high-entropy ceramic. *Ceram Int* 2022, **48**: 23307–23313.

[19] Ding YH, Liu L, Guo RZ, *et al*. $(Hf_{0.25}Zr_{0.25}Sn_{0.25}Ti_{0.25})O_2$ high-entropy ceramics and their microwave dielectric characteristics. *J Am Ceram Soc* 2022, **105**: 6710–6717.

[20] Christoffersen R, Davies PK, Wei XH, *et al*. Effect of Sn substitution on cation ordering in $(Zr_{1-x}Sn_x)TiO_4$ microwave dielectric ceramics. *J Am Ceram Soc* 1994, **77**: 1441–1450.

[21] Park Y. Influence of order–disorder transition on microwave characteristics of tin-modified zirconium titanate. *J Mater Sci Lett* 1995, **14**: 873–875.

[22] Ding YH, Liu L, Yang ZJ, *et al*. Structure and microwave dielectric characteristics of $Hf_{1-x}Ti_xO_2$ ceramics. *J Am Ceram Soc* 2022, **105**: 1127–1135.

[23] Nikiforova GE, Khoroshilov AV, Gavrichev KS, *et al*. Fergusonite–Scheelite phase transition of praseodymium orthoniobate. *Inorg Mater* 2019, **55**: 964–967.

[24] Abreu TO, Abreu RF, do Carmo FF, *et al*. A novel ceramic matrix composite based on $YNbO_4$–TiO_2 for microwave applications. *Ceram Int* 2021, **47**: 15424–15432.

[25] Kim DW, Kwon DK, Yoon SH, *et al*. Microwave dielectric properties of rare-earth ortho-niobates with ferroelasticity. *J Am Ceram Soc* 2006, **89**: 3861–3864.

[26] Hakki BW, Coleman PD. A dielectric resonator method of

measuring inductive capacities in the millimeter range. *IEEE T Microw Theory* 1960, **8**: 402–410.

[27] Yin CZ, Yu ZZ, Shu LL, *et al*. A low-firing melilite ceramic $Ba_2CuGe_2O_7$ and compositional modulation on microwave dielectric properties through Mg substitution. *J Adv Ceram* 2021, **10**: 108–119.

[28] Shannon RD. Revised effective ionic radii and systematic studies of interatomic distances in halides and chalcogenides. *Acta Crystallogr A* 1976, **32**: 751–767.

[29] Zhu JT, Xu J, Zhang P, *et al*. Enhanced mechanical and thermal properties of ferroelastic high-entropy rare-earth-niobates. *Scripta Mater* 2021, **200**: 113912.

[30] Zhang P, Feng YJ, Li Y, *et al*. Thermal and mechanical properties of ferroelastic $RENbO_4$ (RE = Nd, Sm, Gd, Dy, Er, Yb) for thermal barrier coatings. *Scripta Mater* 2020, **180**: 51–56.

[31] Guo WJ, Ma ZY, Luo Y, *et al*. Structure, defects, and microwave dielectric properties of Al-doped and Al/Nd co-doped $Ba_4Nd_{9.33}Ti_{18}O_{54}$ ceramics. *J Adv Ceram* 2022, **11**: 629–640.

[32] Xiao K, Tang Y, Tian YF, *et al*. Enhancement of the cation order and the microwave dielectric properties of $Li_2ZnTi_3O_8$ through composition modulation. *J Eur Ceram Soc* 2019, **39**: 3064–3069.

[33] Blasse G. Vibrational spectra of yttrium niobate and tantalate. *J Solid State Chem* 1973, **7**: 169–171.

[34] Hou JW, Chen Q, Gao C, *et al*. Raman and luminescence studies on phase transition of $EuNbO_4$ under high pressure. *J Rare Earth* 2014, **32**: 787–791.

[35] Sun TL, Chen XM. Raman spectra analysis for $Ba[(Mg_{1-x}Ni_x)_{1/3}Nb_{2/3}]O_3$ microwave dielectric ceramics. *AIP Adv* 2015, **5**: 017106.

[36] Shi F, Dong HL. Vibrational modes and structural characteristics of $(Ba_{0.3}Sr_{0.7})[(Zn_xMg_{1-x})_{1/3}Nb_{2/3}]O_3$ solid solutions. *Dalton Trans* 2011, **40**: 11591–11598.

[37] Feng J, Cheng LJ, Li ZB, *et al*. Structure, B-site short-range ordering and dielectric properties of $Ba(Zn_{1/3}Ta_{2/3})O_3$ microwave ceramics with sub-micron sized grains by spark plasma sintering. *Mater Res Express* 2017, **4**: 066302.

[38] Deng JX, Chen J, Yu RB, *et al*. Crystallographic and Raman spectroscopic studies of microwave dielectric ceramics $Ba(Ca_{1/3}Nb_{2/3})O_3$. *J Alloys Compd* 2009, **472**: 502–506.

[39] Moreira RL, Khalam LA, Sebastian MT, *et al*. Raman-spectroscopic investigations on the crystal structure and phonon modes of $Ba(RE_{1/2}Ta_{1/2})O_3$ microwave ceramics. *J Eur Ceram Soc* 2007, **27**: 2803–2809.

[40] Yang HC, Zhang SR, Wen QY, *et al*. Synthesis of $CaAl_2B_2O_{4+3x}$: Novel microwave dielectric ceramics with low permittivity and low loss. *J Eur Ceram Soc* 2021, **41**: 2596–2601.

[41] Stubičan VS. High-temperature transitions in rare-earth niobates and tantalates. *J Am Ceram Soc* 1964, **47**: 55–58.

[42] Mueller MH, Heaton L, Miller KT. Determination of lattice

parameters with the aid of a computer. *Acta Cryst* 1960, **13**: 828–829.

[43] Ramarao SD, Murthy VRK. Structural phase transformation and microwave dielectric studies of $SmNb_{1-x}(Si_{1/2}Mo_{1/2})_xO_4$ compounds with fergusonite structure. *Phys Chem Chem Phys* 2015, **17**: 12623–12633.

[44] Takei H, Tsunekawa S. Growth and properties of $LaNbO_4$ and $NdNbO_4$ single crystals. *J Cryst Growth* 1977, **38**: 55–60.

[45] Bastide JP. Systématique simplifiée des composés ABX_4 (X = O^{2-}, F^-) et evolution possible de leurs structures cristallines sous pression. *J Solid State Chem* 1987, **71**: 115–120. (in French)

[46] Errandonea D, Manjón FJ. Pressure effects on the structural and electronic properties of ABX_4 scintillating crystals. *Prog Mater Sci* 2008, **53**: 711–773.

[47] Jarry A, Ricote S, Geller A, *et al*. Assessing substitution effects on surface chemistry by *in situ* ambient pressure X-ray photoelectron spectroscopy on perovskite thin films, $BaCe_xZr_{0.9-x}Y_{0.1}O_{2.95}$ (x = 0; 0.2; 0.9). *ACS Appl Mater Interfaces* 2018, **10**: 37661–37670.

[48] Dunyushkina L, Khaliullina A, Meshcherskikh A, *et al*. Effect of A-site nonstoichiometry on defect chemistry and electrical conductivity of undoped and Y-doped $SrZrO_3$. *Materials* 2019, **12**: 1258.

[49] Radenahmad N, Afroze S, Afif A, *et al*. High conductivity and high density $SrCe_{0.5}Zr_{0.35}Y_{0.1}A_{0.05}O_{3-\delta}$ (A = Gd, Sm) proton-conducting electrolytes for IT-SOFCs. *Ionics* 2020, **26**: 1297–1305.

[50] Jian L, Wayman CM. Monoclinic-to-tetragonal phase transformation in a ceramic rare-earth orthoniobate, $LaNbO_4$. *J Am Ceram Soc* 1997, **80**: 803–806.

[51] Shannon RD. Dielectric polarizabilities of ions in oxides and fluorides. *J Appl Phys* 1993, **73**: 348–366.

[52] Tian HR, Zheng JJ, Liu LT, *et al*. Structure characteristics and microwave dielectric properties of $Pr_2(Zr_{1-x}Ti_x)_3(MoO_4)_9$ solid solution ceramic with a stable temperature coefficient. *J Mater Sci Technol* 2022, **116**: 121–129.

[53] Kim ES, Chun BS, Freer R, *et al*. Effects of packing fraction and bond valence on microwave dielectric properties of $A^{2+}B^{6+}O_4$ (A^{2+}: Ca, Pb, Ba; B^{6+}: Mo, W) ceramics. *J Eur Ceram Soc* 2010, **30**: 1731–1736.

[54] Liao QW, Li LX. Structural dependence of microwave dielectric properties of ixiolite structured $ZnTiNb_2O_8$ materials: Crystal structure refinement and Raman spectra study. *Dalton Trans* 2012, **41**: 6963–6969.

[55] Tian HR, Zhou X, Jiang TY, *et al*. Bond characteristics and microwave dielectric properties of $(Mn_{1/3}Sb_{2/3})^{4+}$ doped molybdate based low-temperature sintering ceramics. *J Alloys Compd* 2022, **906**: 164333.

[56] Shi F, Xiao EC. Sintering behavior, crystal structures, phonon characteristics and dielectric properties of $LiZnPO_4$ microwave dielectric ceramics. *Mater Chem Phys* 2021, **259**: 124139.

[57] Su CX, Fang L, Ao LY, *et al*. Correlation between crystal structure and microwave dielectric properties of two garnet-type ceramics in rare-earth-free gallates. *J Eur Ceram Soc* 2021, **41**: 1962–1968.

[58] Hsu TH, Huang CL. Low-loss microwave dielectric of novel $Li_{1−2x}M_xVO_3$ (M = Mg, Zn) (x = 0–0.09) ceramics for ULTCC applications. *J Eur Ceram Soc* 2021, **41**: 5918–5923.

[59] Park HS, Yoon KH, Kim ES. Effect of bond valence on microwave dielectric properties of complex perovskite ceramics. *Mater Chem Phys* 2003, **79**: 181–183.

[60] Brese NE, O'keeffe M. Bond-valence parameters for solids. *Acta Crystallogr B* 1991, **47**: 192–197.

[61] Wu FF, Zhou D, Du C, *et al*. Temperature stable $Sm(Nb_{1−x}V_x)O_4$ (0.0 ⩽ x ⩽ 0.9) microwave dielectric ceramics with ultra-low dielectric loss for dielectric resonator antenna applications. *J Mater Chem C* 2021, **9**: 9962–9971.

[62] Pang LX, Zhou D, Qi ZM, *et al*. Structure–property relationships of low sintering temperature scheelite-structured $(1−x)BiVO_4–xLaNbO_4$ microwave dielectric ceramics. *J Mater Chem C* 2017, **5**: 2695–2701.